Topological orbital angular momentum extraction and twofold protection of vortex transport

Hu, Zhichan; Bongiovanni, Domenico; Wang, Ziteng; Wang, Xiangdong; Song, Daohong; Xu, Jingjun; Morandotti, Roberto; Buljan, Hrvoje; Chen, Zhigang

nature photonics

Article

https://doi.org/10.1038/s41566-024-01564-2

Topological orbital angular momentum extraction and twofold protection of vortex transport

Received: 10 April 2024

Accepted: 7 October 2024

Published online: 20 November 2024

Check for updates

Zhichan Hu[1,5], Domenico Bongiovanni[1,2,5], Ziteng Wang[1,5], Xiangdong Wang[1], Daohong Song[1,3], Jingjun Xu[1] ✉, Roberto Morandotti[2], Hrvoje Buljan[1,4] ✉ & Zhigang Chen[1,3] ✉

Vortex phenomena are ubiquitous in nature. In optics, despite the availability of numerous techniques for vortex generation and detection, topological protection of vortex transport with desired orbital angular momentum (OAM) remains a challenge. Here, by use of topological disclination, we demonstrate a scheme to confine and guide vortices featuring arbitrary high-order charges. Such a scheme relies on twofold topological protection: a non-trivial winding in momentum space due to chiral symmetry, and a non-trivial winding in real space due to the complex coupling of OAM modes across the disclination structure. We unveil a vorticity-coordinated rotational symmetry, which sets up a universal relation between the vortex topological charge and the rotational symmetry order of the system. As an example, we construct photonic disclination lattices with a single core but different C_n symmetries and achieve robust transport of an optical vortex with preserved OAM solely corresponding to one selected zero-energy vortex mode at the mid-gap. Furthermore, we show that such topological structures can be used for vortex filtering to extract a chosen OAM mode from mixed excitations. Our results illustrate the fundamental interplay of vorticity, disclination and higher-order topology, which may open a new pathway for the development of OAM-based photonic devices such as vortex guides, fibres and lasers.

Vortices are observed in a wide range of natural systems, from vortices of quantum particles and living cells to tornados and black holes[1–9]. In optics, vortices are typically characterized by a circulating flux that gives rise to orbital angular momentum (OAM)[10], playing a crucial role in numerous optical phenomena and applications[10–15]. Apart from classical waves, vortex beams carrying OAM have been experimentally realized with photons[3], electrons[4] and even non-elementary particles such as neutrons[5], atoms and molecules[6]. The ability to generate and manipulate vortex beams has sparked substantial scientific interest, leading to research in fundamental phenomena and enabling unconventional implementations across different fields. Like all localized waves, however, vortices of any field tend to spread out during evolution.

Confining vortex flows is important across diverse areas of science and technology. For instance, in free space, localized vortex beams naturally diffract due to their wave nature, making them susceptible to atmospheric turbulence and other environmental factors.

[1]The MOE Key Laboratory of Weak-Light Nonlinear Photonics, TEDA Applied Physics Institute and School of Physics, Nankai University, Tianjin, China. [2]INRS-EMT, Varennes, Quebec, Canada. [3]Collaborative Innovation Center of Extreme Optics, Shanxi University, Taiyuan, China. [4]Department of Physics, Faculty of Science, University of Zagreb, Zagreb, Croatia. [5]These authors contributed equally: Zhichan Hu, Domenico Bongiovanni, Ziteng Wang. ✉e-mail: jjxu@nankai.edu.cn; hbuljan@phy.hr; zgchen@nankai.edu.cn

https://doi.org/10.1038/s41566-024-01564-2

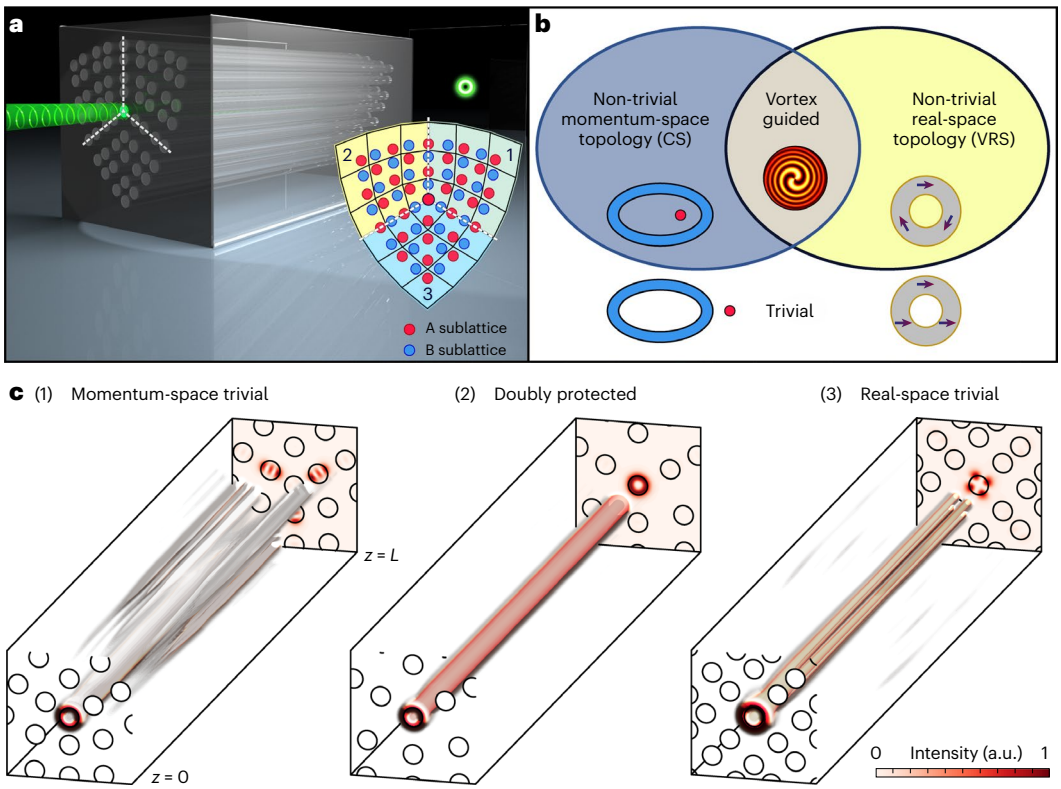

Fig. 1 | Illustration of doubly protected vortex transport via topological disclinations. a, A schematic of a vortex travelling through the core of a disclination lattice that has C_3 rotational symmetry and chiral symmetry (CS). The lattice features two sublattices with a single-site core at the centre, where a vortex is transported, guided and topologically protected. **b**, A Venn diagram of the underlying topology associated with vortex guidance. The light-blue region represents a non-trivial momentum-space winding (illustrated with a non-empty winding loop) as typical for a chiral-symmetric structure. The yellow region represents a non-trivial real-space winding (illustrated with complex coupling vectors winding) when the disclination lattice features a VRS. The overlapping region is where a vortex can have twofold (both real- and momentum-space) topological protection during propagation in a non-trivial disclination structure. **c**, Numerical simulations showing (2) robust propagation of a doubly protected high-order vortex ($l = 2$) to a distance L through the disclination core that serves as a TVG, but (1 and 3) the same vortex expands and breaks up during transport when the twofold protection is absent.

High-order vortices, characterized by topological charges $|l| > 1$, are particularly prone to disintegration during propagation, often breaking up into several 'pieces' of singly charged vortices[16] and further complicating their control and manipulation over long distances. To effectively confine an optical vortex without distortion in shape and preserve its OAM during transport is crucial, particularly for OAM-based optical communications[17]. However, unlike vortex generation and detection[10,11], vortex transport with preserved OAM is a non-trivial task. Addressing this challenge requires innovative approaches in both theoretical design and experimental implementation to create robust and efficient vortex transport systems[17,18].

Recently, there has been a surge of interest in the study of topological disclinations[19–25], unveiling non-trivial topological phases, including higher-order topological phases[26–28]. Topological disclinations, as a representative type of topological defects of a point-group rotational symmetry, can support localized topological states within the bulk[20,21,29] rather than at the boundaries[30]. However, lattice defects and disclinations typically break chiral symmetry, a key element for topological protection in a large family of topological insulators[31]. If disclinations are designed to preserve chiral symmetry, their bounded states can lie exactly in the middle of the bandgap and be pinned at zero energy[24]—reminiscent of Majorana-bound states[19]. Such chiral-symmetric disclinations are ideal for the realization of a topological vortex guide (TVG), where spectral isolation, OAM-mode spatial confinement and topological protection can be guaranteed. Nevertheless, most topological disclination structures established so far, including the recent work on disclination-based vortex nanolasers[32] and solitons[33], consist of a multi-site rather than a single-site core for confining the vortex mode. In curved or engineered three-dimensional (3D) synthetic materials[34–37], localized higher-orbital and vortex states can also emerge, but they rely on complex design of topological defects, and the localized states are not zero-energy OAM modes. In fact, a single-channel TVG has never been realized. In the so-called Dirac-vortex topological structure, the 'vortex' refers to a Kekulé modulation of a Dirac lattice with a vortex phase (as in the Jackiw–Rossi model)[38–40], but the bounded mode itself is not an OAM mode.

Here, we demonstrate a universal principle for the realization of robust vortex transport by using specially designed topological disclination structures. As illustrated in Fig. 1a, a vortex beam preserves its circular shape and phase singularity along the central waveguide—the single-site disclination core in a C_3-rotational and chiral-symmetric lattice. It is 'doubly' protected by both non-trivial momentum-space (k-space) band topology and real-space topology, with the latter characterized by the non-trivial winding of complex vortex-mode coupling (Fig. 1b). The k-space band topology gives rise to the localized mid-gap (zero-energy) vortex states protected by chiral symmetry, while the real-space non-trivial winding ensures the selection of just one OAM mode along the disclination core without the interference from all other possible modes. The principle applies to any high-order OAM modes with topological charge l for any rotational order n of the C_n lattice symmetry, as long as $2l/n$ is not an integer. We unravel this condition as the vorticity-coordinated rotational symmetry (VRS)—essential for the real-space protection of vortex transport in topological disclinations. Experimentally, we employ a laser-writing technique to establish

https://doi.org/10.1038/s41566-024-01564-2

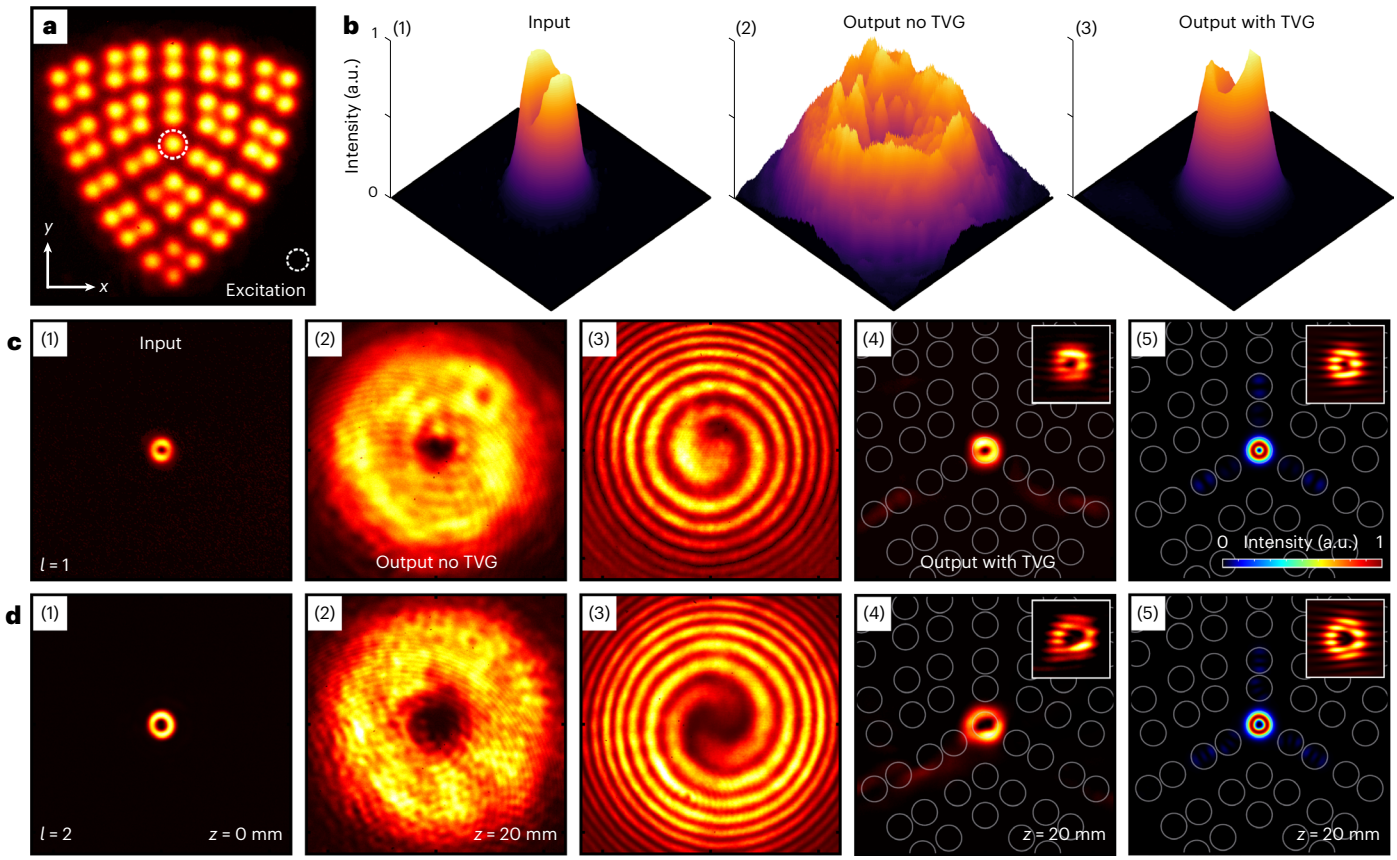

Fig. 2 | Experimental demonstration of vortex transport along a single channel in topological disclination. a, A laser-written photonic lattice featuring C_3-rotational symmetry and chiral symmetry with a single-site disclination core, where a dashed white circle marks the core location for excitation with a vortex beam. **b**, (1–3) 3D intensity plots of the experimental results showing that an input vortex (1) expands dramatically in free space without TVG (2), but it is well guided after propagating through the disclination core with TVG (3). **c**, (1) Intensity pattern of the input vortex beam; (2) output intensity distribution and (3) interferogram of a single-charge $l = 1$ vortex beam after 20 mm of free propagation without the lattice, where the spiral fringes exhibit vorticity; output intensity pattern of the vortex beam after propagating through the disclination lattice from (4) experimental measurement and (5) numerical simulations. **d**, (1–5) Results corresponding to (**c**, 1–5) but obtained for a high-order vortex with a topological charge $l = 2$. The top-right insets in (4) and (5) are interferograms to identify the vortex phase singularity.

different photonic disclination lattices as a test bench and observe that optical vortices with topological charges $l = 1, 2, 3$ can be protected by non-trivial C_3 and C_5 structures, but an $l = 2$ vortex breaks up into a quadrupole-like pattern in the C_4 structure owing to the lack of real-space protection. Numerical simulations (Fig. 1c) further corroborate the conditions needed for protected vortex transport. Moreover, we show that, under a mixed-mode excitation, our topological approach leads to an effective vortex filter, which extracts and protects the transport of a selected OAM mode while filtering out other unwanted modes. Our work represents a demonstration of single-channel TVGs for robust transport of vortices in any system[41].

Results

Our disclination lattices are constructed by 'cutting and gluing'[20,21] a two-dimensional Su–Schrieffer–Heeger (SSH) lattice[42,43] that results in a single-site core at the centre of the structure (Methods and Extended Data Fig. 1). Three disclination lattices featuring C_3-, C_4- and C_5-rotational symmetry are established by laser-writing waveguides in an otherwise uniform crystal (Supplementary Note 1). A typical example of the C_3 disclination and corresponding results are shown in Fig. 2, where Fig. 2a is the disclination lattice. The 3D intensity plots in Fig. 2b(1)–b(3) clearly illustrate the difference between a guided and an unguided vortex. Figure 2c(1) is the input vortex beam with $l = 1$ used to probe the central disclination core. The input beam size is 36 μm, and it expands to about 240 μm after 20 mm propagation through the crystal (without any written waveguide), as seen from the corresponding output intensity pattern (Fig. 2c(2)) and interferogram (Fig. 2c(3)). In contrast, when the same vortex is launched into the disclination core, its intensity is well confined in the core, preserving both the vortex ring pattern and the topological charge (Fig. 2c(4)). Results from numerical simulations (Fig. 2c(5)) agree well with such observations, showing the robustness of the vortex transport even at much longer distances through the vortex guide (Methods, Extended Data Fig. 2 and Supplementary Note 2). Likewise, a high-order vortex with $l = 2$ (Fig. 2d(1)–d(5)) or $l = 3$ (Extended Data Fig. 3) is also well guided in the disclination core.

Protection by momentum-space topology

To understand the essence of the 'double protection' needed for the TVGs, let us first consider the k-space band topology, characterized by the theory of topological invariants in momentum space[31,44]. The band structure of the disclination Hamiltonian considering complex vortex-mode coupling for a C_n-symmetric lattice is calculated using the tight-binding model (Methods and Supplementary Note 4). In our model, the k-space band topology lies in a chiral-symmetric topological phase, which ensures that the topological defect states appear right at zero-energy mid-gap (see Fig. 3a(1),a(2) for $l = 1$ and $l = 2$ cases in the C_3 lattice) and occupy only one sublattice (Fig. 3b(1),b(2),c(1),c(2)). In contrast to photonic crystals or photonic crystal fibres, here the vortex modes are spatially localized modes in the bandgap of

https://doi.org/10.1038/s41566-024-01564-2

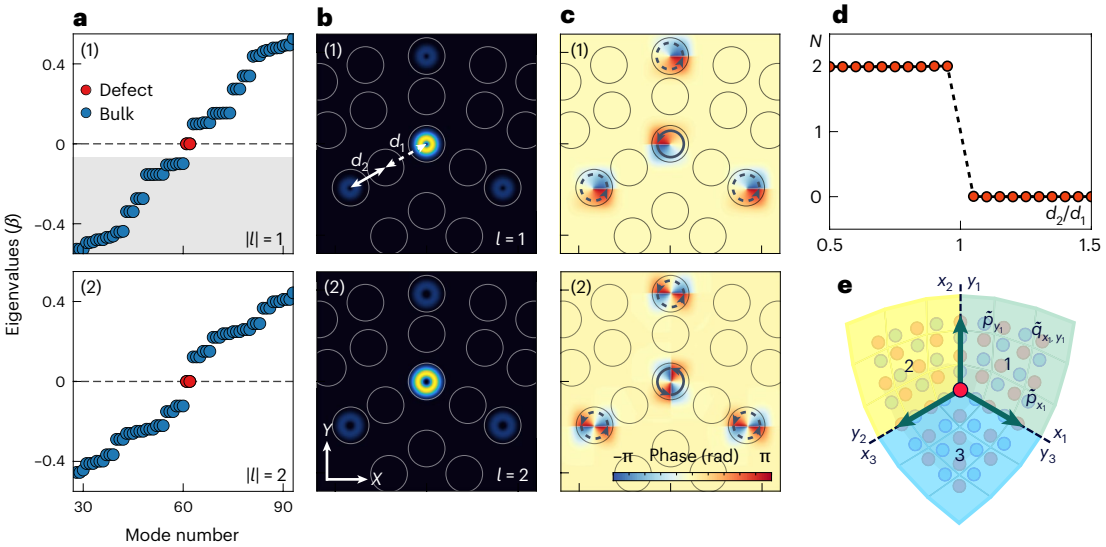

Fig. 3 | Momentum-space protection of zero-energy vortex modes via topological disclination. a, (1) Calculated eigenvalues of single-charge vortex modes in a C_3 chiral-symmetric disclination structure, where two degenerate vortex modes (red) appear right at mid-gap but with opposite vorticity ($l = 1$ and $l = -1$); (2) corresponding results obtained for a pair of high-order ($l = 2$ and $l = -2$) vortex modes in the same C_3 structure. **b**,**c**, (1) Intensity (**b**) and phase (**c**) distributions of the $l = 1$ vortex mode, showing confinement mostly at the disclination core. Exponentially decaying 'tails' distribute only in the same (next-nearest-neighbour) sublattices with a π-phase difference—a characteristic of SSH-type topological states (d_1 and d_2 mark the intra-cell and inter-cell spacing, respectively); (2) corresponding results obtained for a pair of high-order ($l = 2$ and $l = -2$) vortex modes in the same C_3 structure. Note in (**c**, 2) there is a 4π phase circulation for each vortex, and the vortex in the centre again has a π-phase difference compared with those in the 'tails'. **d**, Calculated topological invariant. The MCN N, which equals 2 when d_1 is larger than d_2, indicates a topologically non-trivial regime with two zero-energy disclination modes. **e**, An illustration of multipole moments in the C_3 structure, where $\tilde{q}$ and $\tilde{p}$ are the differences in dipole and quadrupole moments between sublattices, respectively. We show three sets of coordinates (x_i, y_i) with $i = 1, 2, 3$, which correspond to three sectors of the C_3 disclination structure, to generate the multipole operators.

propagation constants, as opposed to time-domain frequencies. The disclination states here cannot be characterized by the topological invariants conventionally used for higher-order topology, for example, the fractional charge density[20,23,27]. To solve this issue, we employ the concept of the multipole chiral number (MCN)[28]. The MCN is a bulk integer topological invariant N recently developed for predicting the number of degenerate zero-energy corner states in higher-order topological systems enriched by chiral symmetry. It is essentially a real-space representation of the winding number generalized from one- to higher-dimensional systems. Since the number of lattice sites belonging to different sublattices in our C_n-symmetric disclination structures are not equal (Fig. 1a), we use N to evaluate the overall difference between the multipole moments of two sublattice wave functions (Fig. 3d,e and Supplementary Note 5). Physically, it describes the winding of the wave function for the B sublattice with respect to the A sublattice. To present the whole structure of a C_n lattice, we use different coordinates for every sector of the C_n lattice to define multipole operators with respect to the central defect and thus get N. The system is topologically non-trivial when $d_2 < d_1$, where the dimerization parameters d_1 and d_2 are the waveguide distances associated with the intra-cell and inter-cell coupling in the SSH model, respectively[28,31,43]. In this case, a non-zero N corresponds to a non-trivial winding in the momentum space, as depicted in Fig. 1b. For example, in Fig. 3d, $N = 2$ indicates that there are two degenerate zero-energy vortex states (Fig. 3a(1),a(2)) with opposite vortex-phase circulation. In contrast, if $d_2 > d_1$, we have $N = 0$ (Fig. 3d), implying a topologically trivial winding and the absence of topological disclination states. Results for other examples of C_n lattices are shown in Extended Data Fig. 4. This generalized MCN can be applied to characterize higher-order topological phases in other non-periodic C_n-symmetric structures that exhibit chiral symmetry. Results in Fig. 3 highlight one key ingredient needed for protecting the vortex transport: momentum-space topology featured by chiral symmetry of the disclination structure. The role of chiral symmetry is to guarantee that the guided vortex mode is at zero energy. In practice, even if the mode is not exactly at the middle of the bandgap, it can still enjoy topological protection if it resides close to the mid-gap.

Protection by real-space topology

Notwithstanding that there are two degenerate zero-energy vortex modes, robust transport of a vortex requires that only a single vortex state be present at the disclination core during propagation. Every waveguide can support both clockwise ($l < 0$) and anti-clockwise ($l > 0$) phase circulations; thus, there are two types of vortex mode coupling between waveguides (Fig. 4a(1)): the same-vorticity mode coupling (SVMC), which is always real regardless of the coupling direction, and the direction-dependent opposite-vorticity mode coupling (OVMC). The OVMC can be illustrated by a coupling vector t_{OV} (Supplementary Note 4) in the complex plane (Fig. 4a(2)). To ensure that a TVG supports only a single clockwise (or anti-clockwise) vortex mode at any propagation distance, no anti-clockwise (or clockwise) components should arise at the disclination core during the transport, as analysed in Supplementary Note 6. This indicates that the collective contribution of the OVMC from all waveguides across the entire lattice to the disclination core must be zero.

In a C_n disclination lattice, we evaluate the OVMC between the core and all other waveguides belonging to each distinct sector and then examine the winding of the complex coupling T_j from each of the n rotational sectors (see Fig. 4b(1)–b(3) for the C_3 lattice, Fig. 4c(1)–c(3) for the C_4 lattice and Fig. 4d(1)–d(3) for the C_5 lattice). Real-space topology can be examined by defining a coupling winding number as

$$w = \frac{1}{2\pi i}\sum_{j=1}^{n} \ln\left(\frac{T_{j+1}}{T_j}\right). \quad (1)$$

We find that w is non-zero only when $2l/n$ is not an integer number, indicating the existence of a topologically non-trivial phase. In this

https://doi.org/10.1038/s41566-024-01564-2

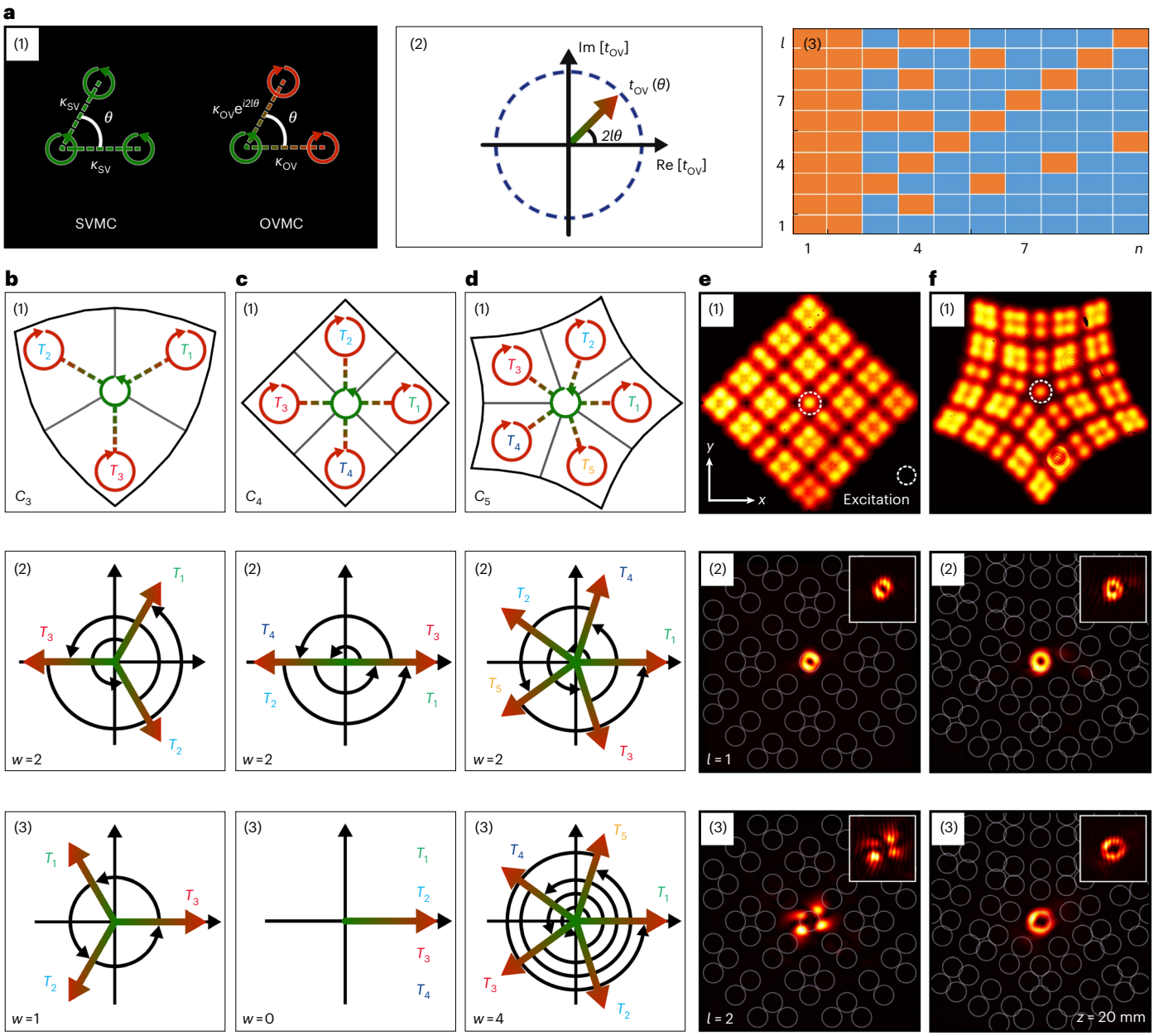

Fig. 4 | Real-space protection of vortex transport and universal rule for VRS-mediated non-trivial winding. a, (1, 2) An illustration of two types of vortex mode coupling between two waveguides where κ is the coupling amplitude; the SVMC is not direction dependent (1), while the OVMC features a coupling coefficient t_{OV} dependent on θ as plotted in (2). **b**–**d**, In a C_n-symmetric disclination structure, all coupling contributions to the central vortex mode can be calculated by sectors as illustrated for C_3 (**b**, 1–3), C_4 (**c**, 1–3) and C_5 (**d**, 1–3) disclination structures, where T_j is the equivalent coupling for all OVMCs in each sector; (**b**, 1) depicts the collective OVMC coupling from the three sectors, (**b**, 2,3) represent real-space winding for charges 1 and 2 vortices in the C_3 disinclination, and (**c**, 1–3) and (**d**, 1–3) follow the same layout as (**b**, 1–3) but are for C_4 and C_5 disclinations, respectively. To guarantee that only a single vortex mode ($l = 1$ in the third row; $l = 2$ in the fourth row) is present at the disclination core, the complex coupling T_j must have a non-zero winding number ($w \neq 0$), as shown. This is better described by the VRS that demands a non-integer value of $2l/n$ for twofold protection, as summarized in **a** (3), where blue (orange) indicates protected (unprotected) vortex modes. Taking $l = 2$ as an example, the vortex is protected in the C_3 disclination owing to non-trivial winding $w = 1$ (**b**, 3), but it is not protected in the C_4 disclination since $2l/n = 1$ is an integer and $w = 0$ in this case (**c**, 3). A vortex is topologically protected only under non-zero winding conditions. **e**,**f**, Experimental results obtained from C_4 (**e**, 1) and C_5 (**f**, 1) disclination structures, which show that, as in C_3 disclination (Fig. 2), both $l = 1$ (**f**, 2) and $l = 2$ (**f**, 3) vortices are also protected in the C_5 disclination, however, in the C_4 disclination, the $l = 1$ vortex is protected (**e**, 2) but the $l = 2$ vortex is not protected (**e**, 3), in agreement with the winding picture and the relation plotted in **a** (3).

case, we have the total complex coupling $\sum_{j=1}^{n} T_j = 0$. On the contrary, when $2l/n$ is an integer, w becomes zero and also $\sum_{j=1}^{n} T_j \neq 0$ (Supplementary Note 7). In the examples of C_3 and C_5 lattices, the coupling winding is found to be non-zero for both $l = 1$ and $l = 2$, thus resulting in protected vortex transport (Figs. 2 and 4f(1)–f(3)). However, in the C_4 lattice (Fig. 4e(1)), the winding is non-zero for $l = 1$ but vanishes for $l = 2$. As such, the C_4 lattice can stably guide a single-charge vortex (Fig. 4e(2)) but not a double-charge vortex. In the latter case, the $l = 2$ vortex breaks up into a quadrupole-like pattern (Fig. 4e(3)), in agreement with simulation results (Fig. 1c and Extended Data Fig. 2). This winding picture (see also Fig. 1b) resembles the skyrmion-like spin texture in a magnetic structure[45]. Here, the non-trivial real-space

https://doi.org/10.1038/s41566-024-01564-2

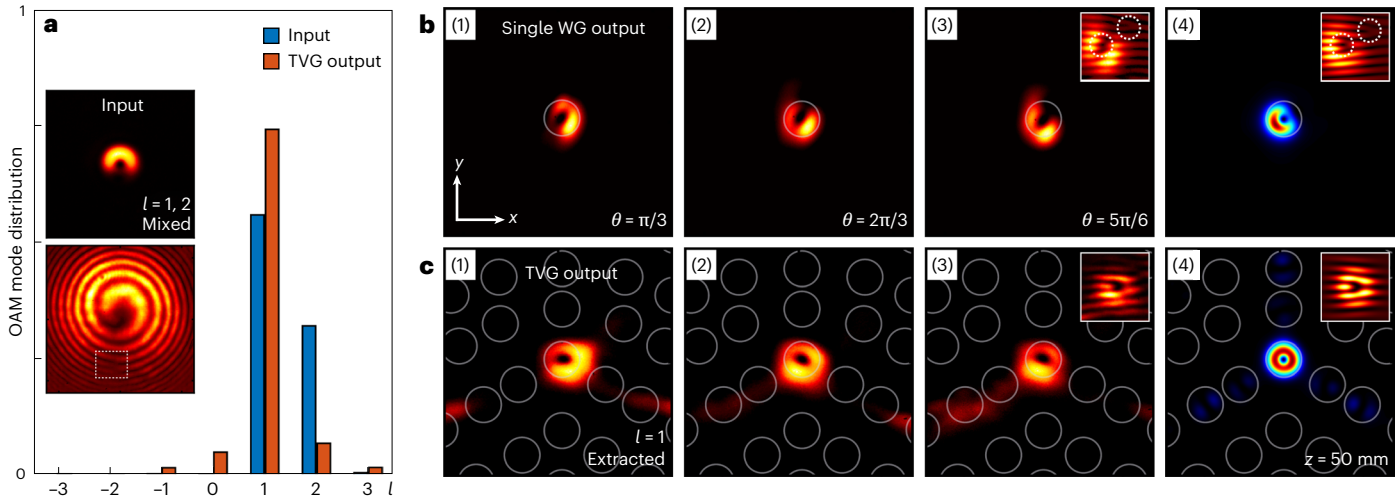

Fig. 5 | OAM extraction (filtering) from mixed-mode excitation via topological disclination. a, A comparison of the OAM-mode distribution between input and output (after exiting the TVG) under mixed excitation, which is obtained by projecting the experimentally measured results onto the calculated OAM eigenmodes of the waveguide; the insets show the input intensity pattern (top) and the corresponding interferogram (bottom) for a mixed-mode ($l = 1$ and $l = 2$) excitation. **b**, Output from a single waveguide under mixed excitation. The intensity ratio between the two modes determines the overall output pattern, which changes and rotates as the relative phase is varied from (1) π/3 and (2) 2π/3 to (3) 5π/6 (the $l = 2$ vortex cannot be eliminated during propagation, leading to an overall broken vortex pattern); (4) corresponding simulations. **c**, (1–3) Output from the C_3 disclination under the same excitation corresponding to (**b**, 1–3), showing that the $l = 2$ vortex is filtered out (due to that the structure is made in this case topologically trivial for the $l = 2$ mode, although the VRS is still valid), whereas the protected $l = 1$ mode is preserved; (4) corresponding simulations. In **b** (4) and **c** (4), the corresponding simulations confirm that the protected vortex preserves its shape and undergoes robust propagation along the disclination core—even for long distances (**c**, 4), in contrast to what happens in a single waveguide (**b**, 4) (Supplementary Media File (1)). The top-right insets are interferograms obtained to identify the vortex phase singularity.

winding of the complex coupling vectors depends on the lattice rotational symmetry order n with respect to the vortex topological charge l for a chosen OAM mode. For this reason, we name it vorticity-coordinated rotational symmetry (VRS). Although not easily visualized in a simple picture, we can consider the VRS intuitively as follows. For a given clockwise (or counter-clockwise) vortex mode excitation at the disclination core, coupling along an arbitrary closed path in the C_n disclination structure will not induce counter-clockwise (or clockwise) vortex modes when coming back to the disclination core. This is guaranteed by real-space topology: one can always find other corresponding paths in the structure that are equivalent up to a rotation by $2\pi/n$, such that the interference of all these OVMC paths is zero, which in turn protects the excited vortex mode. Hence, the VRS can be thought of as a rotational symmetry that coordinates with the vorticity of the optical field, and it sets up a universal rule for real-space protection of a single high-order vortex (with either clockwise or anti-clockwise phase circulation but without mixing) propagating along the C_n disclination core.

We further explore the general cases featuring arbitrary n and l and theoretically prove that the total complex couplings accounting for the OVMC between the central defect waveguide and all contributions originating from n sectors vanish if and only if the winding number is non-zero, which requires a non-integer $2l/n$ (Supplementary Notes 6 and 7). Such a condition (summarized in Fig. 4a(3)) sets up a universal rule for protecting the transport of a single high-order vortex (with either clockwise or anti-clockwise phase circulation but not both) along the C_n disclination core (Supplementary Note 8). By considering the alternative example of a C_5 disclination for even higher topological charges, we show that a vortex beam with $l = 5$ or $l = 10$ cannot maintain its shape during propagation, but other high-order OAM modes are well guided as long as $2l/5$ is non-integer (Extended Data Fig. 5), further validating the established condition. Results in Fig. 4 highlight another key ingredient needed for protecting the vortex transport: real-space topology mediated by the VRS of the disclination structure.

Topological extraction of an OAM mode

The presented features of real and momentum-space topology can be readily employed to single out a selected OAM mode (non-trivial) from a mixed-mode excitation, while other modes (trivial) dissipate into the bulk. In Fig. 5, we show a proof-of-concept demonstration. For a mixed excitation of $l = 1$ and $l = 2$ modes, by judiciously choosing the lattice parameters (Supplementary Note 3), we achieve different transport dynamics of the OAM modes through a single waveguide versus a disclination structure: in a single waveguide, beating between $l = 1$ and $l = 2$ modes leads to a strongly deformed and unstable vortex pattern (Fig. 5b(1)–b(4)), whereas, in the TVG, the $l = 2$ mode is 'filtered' out but the $l = 1$ mode is preserved during transport (Fig. 5c(1)–c(4)). In Fig. 5a, we also plot the modal weighting into the OAM basis (OAM mode distribution) before (blue) and after (red) filtering takes place, which clearly shows that the $l = 2$ mode is suppressed after propagating through the TVG, especially when compared with a single waveguide that does not have any filtering (Methods). These experimental results along with numerical simulations clearly demonstrate that topological disclinations can be implemented to extract and transport a desired OAM mode, promising for structure-based vortex filters.

Discussion

We have demonstrated the fundamental principle behind OAM mode extraction and twofold protection of vortex transport via chiral-symmetric topological disclinations. The principle allows for robust guidance of a single zero-energy vortex mode, or for selection of one of the degenerate OAM modes from mixed-mode excitations, which cannot be achieved in topologically trivial waveguide structures including specially designed optical fibres[12,17]. Even if the structure has non-trivial topology in momentum space, that is, it supports zero-energy mode due to chiral symmetry inherent to the SSH-like system, it can support and protect an OAM mode only when the VRS is also satisfied. This reflects the interplay of vorticity, symmetry and topological phases. Detailed stability analyses under different perturbations (respecting chiral symmetry, subsymmetry[46] and rotational

symmetry) are presented in Supplementary Notes 9 and 10, confirming the advantage of twofold protection from the TVG approach. In Supplementary Note 11, we show how a high-order vortex ($l = 5$) remains guided (no diffraction, no splitting) in the TVG, however it dramatically diffracts and breaks up into multiple $l = 1$ vortices under the same perturbation in the absence of a waveguide (Extended Data Fig. 6 and Supplementary Media File (3)).

Over the past decades, guiding light has been based on the paradigm of either total internal reflection or photonic bandgaps, but recent exploration has heralded new mechanisms for unconventional transport, including, for example, guiding light by geometric phases[47], by centrifugal barriers from the OAM of light itself[48] and by optical Coriolis forces around the Lagrange points[49]. Our topological approach certainly opens a new avenue for guiding light, particularly for protected vortex transport.

While this work focuses mainly on the fundamental principle, it may bring about a solution to the long-standing challenge of controlling vortex transport applicable to different fields, since the underlying physics for topological protection of vortices is broadly valid. For instance, it may be applied to acoustics and topolectrical circuitry where chiral symmetry has already been realized[24,50,51]. In technologically important structures like photonic crystals, recent work has demonstrated that photonic crystal fibres can be designed to host topological supermodes across multiple cores[52]. Thus, we envision that our scheme may be adopted for the design of microstructured optical fibres enabling protection of OAM modes in future communication networks[17]. With the rapid advancement of integrated vortex generation[11,32,53,54], the topological approach may open a pathway for routing and protecting vortices, particularly classical and quantum OAM modes, from one place to another with unprecedented transport properties.

Online content

Any methods, additional references, Nature Portfolio reporting summaries, source data, extended data, supplementary information, acknowledgements, peer review information; details of author contributions and competing interests; and statements of data and code availability are available at https://doi.org/10.1038/s41566-024-01564-2.

References

1. Matthews, M. R. et al. Vortices in a Bose–Einstein condensate. *Phys. Rev. Lett.* **83**, 2498–2501 (1999).
2. Zwierlein, M. W. et al. Vortices and superfluidity in a strongly interacting Fermi gas. *Nature* **435**, 1047–1051 (2005).
3. Mair, A. et al. Entanglement of the orbital angular momentum states of photons. *Nature* **412**, 313–316 (2001).
4. Uchida, M. & Tonomura, A. Generation of electron beams carrying orbital angular momentum. *Nature* **464**, 737–739 (2010).
5. Clark, C. W. et al. Controlling neutron orbital angular momentum. *Nature* **525**, 504–506 (2015).
6. Luski, A. et al. Vortex beams of atoms and molecules. *Science* **373**, 1105–1109 (2021).
7. Wioland, H. et al. Confinement stabilizes a bacterial suspension into a spiral vortex. *Phys. Rev. Lett.* **110**, 268102 (2013).
8. The Event Horizon Telescope Collaboration et al. First Sagittarius A* Event Horizon Telescope results. VII. Polarization of the ring. *Astrophys. J.* **964**, L26 (2024).
9. Nye, J. F. & Berry, M. V. Dislocations in wave trains. *Proc. R. Soc. Lond. A* **336**, 165–190 (1974).
10. Shen, Y. et al. Optical vortices 30 years on: OAM manipulation from topological charge to multiple singularities. *Light Sci. Appl.* **8**, 90 (2019).
11. Ni, J. et al. Multidimensional phase singularities in nanophotonics. *Science* **374**, eabj0039 (2021).
12. Bozinovic, N. et al. Terabit-scale orbital angular momentum mode division multiplexing in fibers. *Science* **340**, 1545–1548 (2013).
13. Miao, P. et al. Orbital angular momentum microlaser. *Science* **353**, 464–467 (2016).
14. Yang, Z. Q. et al. Spin-momentum-locked edge mode for topological vortex lasing. *Phys. Rev. Lett.* **125**, 013903 (2020).
15. Bahari, B. et al. Photonic quantum hall effect and multiplexed light sources of large orbital angular momenta. *Nat. Phys.* **17**, 700–703 (2021).
16. Soskin, M. S. et al. Topological charge and angular momentum of light beams carrying optical vortices. *Phys. Rev. A* **56**, 4064–4075 (1997).
17. Willner, A. E. et al. Orbital angular momentum of light for communications. *Appl. Phys. Rev.* **8**, 041312 (2021).
18. Lian, Y. et al. OAM beams generation technology in optical fiber: a review. *IEEE Sens. J.* **22**, 3828–3843 (2022).
19. Teo, J. C. & Hughes, T. L. Existence of Majorana–Fermion bound states on disclinations and the classification of topological crystalline superconductors in two dimensions. *Phys. Rev. Lett.* **111**, 047006 (2013).
20. Peterson, C. W. et al. Trapped fractional charges at bulk defects in topological insulators. *Nature* **589**, 376–380 (2021).
21. Liu, Y. et al. Bulk-Disclination correspondence in topological crystalline insulators. *Nature* **589**, 381–385 (2021).
22. Wang, Q. et al. Observation of protected photonic edge states induced by real-space topological lattice defects. *Phys. Rev. Lett.* **124**, 243602 (2020).
23. Li, T. et al. Fractional disclination charge in two-dimensional C_n-symmetric topological crystalline insulators. *Phys. Rev. B* **101**, 115115 (2020).
24. Deng, Y. et al. Observation of degenerate zero-energy topological states at disclinations in an acoustic lattice. *Phys. Rev. Lett.* **128**, 174301 (2022).
25. Lin, Z.-K. et al. Topological phenomena at defects in acoustic, photonic and solid-state lattices. *Nat. Rev. Phys.* **5**, 483–495 (2023).
26. Benalcazar, W. A., Bernevig, B. A. & Hughes, T. L. Quantized electric multipole insulators. *Science* **357**, 61–66 (2017).
27. Peterson, C. W. et al. A fractional corner anomaly reveals higher-order topology. *Science* **368**, 1114–1118 (2020).
28. Benalcazar, W. A. & Cerjan, A. Chiral-symmetric higher-order topological phases of matter. *Phys. Rev. Lett.* **128**, 127601 (2022).
29. Lustig, E. et al. Photonic topological insulator induced by a dislocation in three dimensions. *Nature* **609**, 931–935 (2022).
30. Noh, J. et al. Topological protection of photonic mid-gap defect modes. *Nat. Photon.* **12**, 408–415 (2018).
31. Ozawa, T. et al. Topological photonics. *Rev. Mod. Phys.* **91**, 015006 (2019).
32. Hwang, M.-S. et al. Vortex nanolaser based on a photonic disclination cavity. *Nat. Photon.* **18**, 286–293 (2023).
33. Huang, C. et al. Vortex solitons in topological disclination lattices. Nanophotonics 10.1515/nanoph-2023-0790) (2024).
34. Chen, Y. et al. Observation of topological *p*-orbital disclination states in non-Euclidean acoustic metamaterials. *Phys. Rev. Lett.* **129**, 154301 (2022).
35. Wang, Q. et al. Vortex states in an acoustic Weyl crystal with a topological lattice defect. *Nat. Commun.* **12**, 3654 (2021).
36. Ran, Y., Zhang, Y. & Vishwanath, A. One-dimensional topologically protected modes in topological insulators with lattice dislocations. *Nat. Phys.* **5**, 298–303 (2009).
37. Lin, Z. K. et al. Topological Wannier cycles induced by sub-unit-cell artificial gauge flux in a sonic crystal. *Nat. Mater.* **21**, 430–437 (2022).
38. Gao, X. et al. Dirac-vortex topological cavities. *Nat. Nanotechnol.* **15**, 1012–1018 (2020).
39. Menssen, A. J. et al. Photonic topological mode bound to a vortex. *Phys. Rev. Lett.* **125**, 117401 (2020).

40. Ma, J. et al. Nanomechanical topological insulators with an auxiliary orbital degree of freedom. *Nat. Nanotechnol.* **16**, 576–583 (2021).
41. Hu, Z. et al. Topological guidance of vortices by disclination. In *Conference on Lasers and Electro-Optics Optics* paper FM2B.3 (OSA, 2023).
42. Liu, F. & Wakabayashi, K. Novel topological phase with a zero berry curvature. *Phys. Rev. Lett.* **118**, 076803 (2017).
43. Hu, Z. et al. Nonlinear control of photonic higher-order topological bound states in the continuum. *Light Sci. Appl.* **10**, 164 (2021).
44. Hasan, M. Z. & Kane, C. L. Colloquium: topological insulators. *Rev. Mod. Phys.* **82**, 3045–3067 (2010).
45. Togawa, Y. et al. Chiral magnetic soliton lattice on a chiral Helimagnet. *Phys. Rev. Lett.* **108**, 107202 (2012).
46. Wang, Z. et al. Sub-symmetry-protected topological states. *Nat. Phys.* **19**, 992–998 (2023).
47. Slussarenko, S. et al. Guiding light via geometric phases. *Nat. Photon.* **10**, 571–575 (2016).
48. Ma, Z., Kristensen, P. & Ramachandran, S. Scaling information pathways in optical fibers by topological confinement. *Science* **380**, 278–282 (2023).
49. Luo, H. et al. Guiding Trojan light beams via lagrange points. *Nat. Phys.* **20**, 95–100 (2024).
50. Wang, D. et al. Realization of a *Z*-classified chiral-symmetric higher-order topological insulator in a coupling-inverted acoustic crystal. *Phys. Rev. Lett.* **131**, 157201 (2023).
51. Imhof, S. et al. Topolectrical-circuit realization of topological corner modes. *Nat. Phys.* **14**, 925–929 (2018).
52. Roberts, N. et al. Topological supermodes in photonic crystal fiber. *Sci. Adv.* **8**, eadd3522 (2022).
53. Chen, B. et al. Integrated optical vortex microcomb. *Nat. Photon.* **18**, 625–631 (2024).
54. Liu, Y. et al. Integrated vortex soliton microcombs. *Nat. Photon.* **18**, 632–637 (2024).

Methods

Construction of single-site disclination lattices

The C_n-symmetric disclination used in this work is constructed by a modified cutting and gluing procedure[20,21]. Compared with previous lattice structures derived from the standard two-dimensional SSH model[42], our disclination structure is uniquely designed to have a single-site core, yet featuring chiral symmetry.

As illustrated in Extended Data Fig. 1a,b, the conventional disclination structures belong to either the type-I or type-II categories[20,21]. The type of disclination is identified by the amount of translation and rotation of a vector around a chosen path (depending on the translation value $[\mathbf{a}]$ and the Frank angle Ω)[23]. Type-I disclination lattices with Frank angle $\Omega = -90°$ and the holonomy value of a closed path around the core $[\mathbf{a}]^{(4)} = 0$ are terminated by weak bonds at the centre location (Extended Data Fig. 1a). Complementarily, type-II lattices with $\Omega = -90°$ and $[\mathbf{a}]^{(4)} = 1$ have strong bonds around the defect core (Extended Data Fig. 1b). In the non-trivial phase, the Wannier centres (quadrangular yellow stars) are positioned at the intersection among four-unit cells. We note that chiral symmetry is not present in both types of disclination[20].

The C_n disclination with a single-site core used in our work cannot be simply categorized as one of the above classes, and its formation requires the removal of some lattice sites instead of just cutting and gluing. To guarantee the existence of zero-energy bound states, we appropriately modify an initial type-II disclination structure. The resulting lattice displays three-unit cells composed of four sites intersecting at the centre, each of which belongs to one of the C_3-symmetric sectors (Extended Data Fig. 1c). We first shift every lattice sector with respect to the core until the three nearest waveguides perfectly overlap. The white arrows in the inset indicate the directions to shift the lattice sites. Then, any overlapped (extra) lattice sites that break chiral symmetry in the traditional disclination structure are removed, so that the array index is still uniform. In a similar way, other C_n-symmetric lattices can be readily constructed. A characteristic difference between our scheme and those previously shown type-I and type-II disclinations is that our single-core C_n disclinations possess chiral symmetry and can thus support topologically protected zero-energy bound states.

Discrete vortex Hamiltonian

In the OAM domain, we express the real-space Hamiltonian of a C_n-symmetric disclination lattice with topological charge l under the tight-binding approximation as

$$H = \sum_{\mathbf{R},\mathbf{R}',l} \xi(\mathbf{R}-\mathbf{R}')\left[\kappa_{\mathrm{SV}} c^{\dagger}_{\mathbf{R},l} c_{\mathbf{R}',l} + \kappa_{\mathrm{OV}} \mathrm{e}^{2il\theta(\mathbf{R}-\mathbf{R}')} c^{\dagger}_{\mathbf{R},l} c_{\mathbf{R}',-l}\right], \qquad \text{(M1)}$$

where $\xi(\mathbf{R}-\mathbf{R}') = \mathrm{e}^{-\rho|\mathbf{R}-\mathbf{R}'|}$ is the hopping amplitude between two nearest-neighbour waveguides of the C_n-disclination lattice located at the positions $\mathbf{R}$ and $\mathbf{R}'$, and ρ is a scale factor. The hopping amplitudes are approximated as an exponential decay function of the difference $|\mathbf{R}-\mathbf{R}'|$ (ref. 55). The parameter κ_{SV} describes the SVMC, while κ_{OV} describes the OVMC, with $\theta(\mathbf{R}-\mathbf{R}')$ being the azimuth angle of the vector $\mathbf{R}-\mathbf{R}'$. $c^{\dagger}_{\mathbf{R},l}$ is the creation operator at the lattice site with position $\mathbf{R}$, corresponding to a vortex mode with a topological charge l. An analogous definition is given for the annihilation operators. The vortex band structures reported in Fig. 3 are calculated by diagonalizing H for the same C_3-disclination structure, but distinct l values. Related vortex-mode distributions are found by retrieving both clockwise ($l < 0$) and anti-clockwise ($l > 0$) components from the calculated eigenvectors of H.

Experimental methods

We create three disclination photonic lattices with C_3-, C_4- and C_5-rotational symmetries by employing a site-to-site CW-laser-writing technique in a 20-mm-long photorefractive crystal[43,56]. For the C_3 lattice shown in Fig. 2a, the intra-cell and inter-cell waveguide distances (corresponding to d_1 and d_2 in Fig. 3b(1)) are, respectively, 57.5 μm and 42.5 μm for guiding the $l = 1$ vortex, and 69 μm and 51 μm for guiding the $l = 2$ vortex. In the writing process, an ordinary-polarized laser beam with a 532 nm wavelength and a low power of about 70 mW is phase-modulated in the Fourier domain by a spatial light modulator, to create a quasi-non-diffracting beam at variable writing positions. Every waveguide remains intact during each set of measurements owing to the photorefractive 'memory effect'[43,56]. The probing process is performed by launching into the disclination core an extraordinary-polarized vortex beam at the same wavelength with different topological charges. The probe vortex is generated by imposing a helical phase together with an amplitude modulation on a Gaussian-like beam assisted with the spatial light modulator, which can be described as $\Psi(x,y,0) = Ar^{|l|}\exp(-\frac{r^2}{w^2})\exp(il\varphi)$. This indicates that the probe beam features a high-order vortex with a topological charge l (here, A is an amplitude parameter, $r = \sqrt{x^2+y^2}$ and $\varphi = \tan^{-1}(y/x)$ are the radial and azimuthal coordinates, while w is a normalization width). Such generated vortices resemble the Laguerre–Gauss beams that carry OAM. Experimentally, interferograms are obtained by setting the interference between the vortex beam and a reference quasi-plane wave or spherical wave to identify the vorticity (see Supplementary Note 1 for more details). Numerically, we calculate the guided modes (eigenmodes) of individual waveguides in the disclination structure using experimental parameters and find that the mode profiles well fit those of Laguerre–Gauss modes. Thus, since the excitation beam is modulated to have radial modes approximately matching the eigenmodes, it will evolve into a disclination vortex mode during propagation through the structure with preserved OAM.

To demonstrate OAM filtering from a mixed-mode excitation, in Fig. 5, we plot the modal weighting into the OAM basis (OAM mode distribution) before and after the filtering from our experimental results. The OAM spectrum is obtained by calculating $|\langle\Psi_{\mathrm{exp}}|\Psi_l\rangle|^2$, where Ψ_{exp} is the amplitude of the light field from the experimental output beam in the disclination core, and Ψ_l is the eigenmode of our photonic waveguide obtained from numerical simulations (with an induced index change $\Delta n/n = 1.11\times10^{-4}$ and a waveguide width 36 μm; similar to our experimental condition). Both Ψ_{exp} and Ψ_l are normalized so that $|\langle\Psi_{\mathrm{exp}}|\Psi_{\mathrm{exp}}\rangle|^2 = |\langle\Psi_l|\Psi_l\rangle|^2 = 1$. The possible OAM modes involved under this condition are $l = -3, -2, -1, +1, +2, +3$. The amplitude of the experimental output is directly acquired from the charged-coupled device (CCD) image, with its corresponding phase measured through the plane-wave interferogram using the method previously established[57]. Due to the limitation of the method (projecting experimental data onto the eigenmodes calculated for an ideal single waveguide) to attain the OAM spectrum, small portions of initially unexcited modes (for example, $l = 0$) appear to be present at output, but in reality, these modes are not involved.

Numerical methods

The propagation dynamics of an optical vortex beam are simulated using a continuum model of the nonlinear Schrödinger-like equation (NLSE)[46]

$$i\frac{\partial\Psi}{\partial z} = -\frac{1}{2k}\nabla_{\perp}^2\Psi - \frac{k\Delta n_0}{n_0}\frac{\Psi}{1+I_{\mathrm{L}}(x,y)+I_{\mathrm{P}}(x,y)}, \qquad \text{(M2)}$$

where $\Psi(x,y,z)$ is the electric field envelope, x and y denote the transverse coordinates, z is the longitudinal propagation distance and $\nabla_{\perp}^2 = \partial^2/\partial x^2 + \partial^2/\partial y^2$ is the transversal Laplacian operator. Here, k is the wavenumber in the medium, $n_0 = 2.35$ is the refractive index for our specific photorefractive crystal and $\Delta n_0 = -n_0^3 r_{33} E_0/2$ is the refractive-index change, where $r_{33} = 280$ pm V^{-1} is the electro-optic coefficient along the crystalline c axis, and E_0 is the bias electric field. The two terms $I_{\mathrm{L}}(x,y)$ and $I_{\mathrm{P}}(x,y)$ denote the intensity patterns of the

lattice-writing and lattice-probing beams, respectively. To confirm the theoretical prediction of TVG formation in the proposed C_n-disclination lattice, experimental measurements are also corroborated by numerical simulations using the NLSE in equation (M2) (Supplementary Note 2). For a linear vortex-beam excitation, the NLSE solutions are found via a split-step Fourier transform method under the condition that $I_P(x, y, z)$ is weak, so the probe beam itself does not undergo nonlinear self-action during propagation.

Data availability

Data supporting key conclusions of this work are included within the Article and its Supplementary Information. All other raw data that support the findings of this study are available from the corresponding authors on reasonable request.

References

55. Jörg, C. et al. Artificial gauge field switching using orbital angular momentum modes in optical waveguides. *Light Sci. Appl.* **9**, 150 (2020).
56. Xia, S. et al. Unconventional flatband line states in photonic lieb lattices. *Phys. Rev. Lett.* **121**, 263902 (2018).
57. Takeda, M., Ina, H. & Kobayashi, S. Fourier-transform method of fringe-pattern analysis for computer-based topography and interferometry. *J. Opt. Soc. Am.* **72**, 156–160 (1982).

Acknowledgements

We thank Y. Kartashov and A. Cerjan for their valuable discussions. D.S. and Z.C. acknowledge funding from the National Key R&D Program of China (grant no. 2022YFA1404800) the National Natural Science Foundation of China (grant nos. 12134006 and 12274242). Z.H. acknowledges the support of China Postdoctoral Science Foundation (grant no. BX20240174). H.B. acknowledges support from the QuantiXLie Center of Excellence, a project co-financed by the Croatian Government and European Union through the European Regional Development Fund – the Competitiveness and Cohesion Operational Programme. R.M. acknowledges support from NSERC and the CRC programme in Canada.

Author contributions

Z.C. conceived the project. Z.H. and D.B. conducted the experiments. Z.W. and H.B. developed the theoretical framework and numerical simulations of the discrete models. D.B. and Z.H. performed numerical simulations of the continuous models. X.W., D.S. and J.X. contributed to the discussion of results. Z.C., H.B. and R.M. supervised the project. All authors contributed to this work.

Competing interests

The authors declare no conflicts of interest.

Additional information

Extended data is available for this paper at https://doi.org/10.1038/s41566-024-01564-2.

Supplementary information The online version contains supplementary material available at https://doi.org/10.1038/s41566-024-01564-2.

Correspondence and requests for materials should be addressed to Jingjun Xu, Hrvoje Buljan or Zhigang Chen.

Peer review information *Nature Photonics* thanks Baile Zhang and the other, anonymous, reviewer(s) for their contribution to the peer review of this work.

https://doi.org/10.1038/s41566-024-01564-2

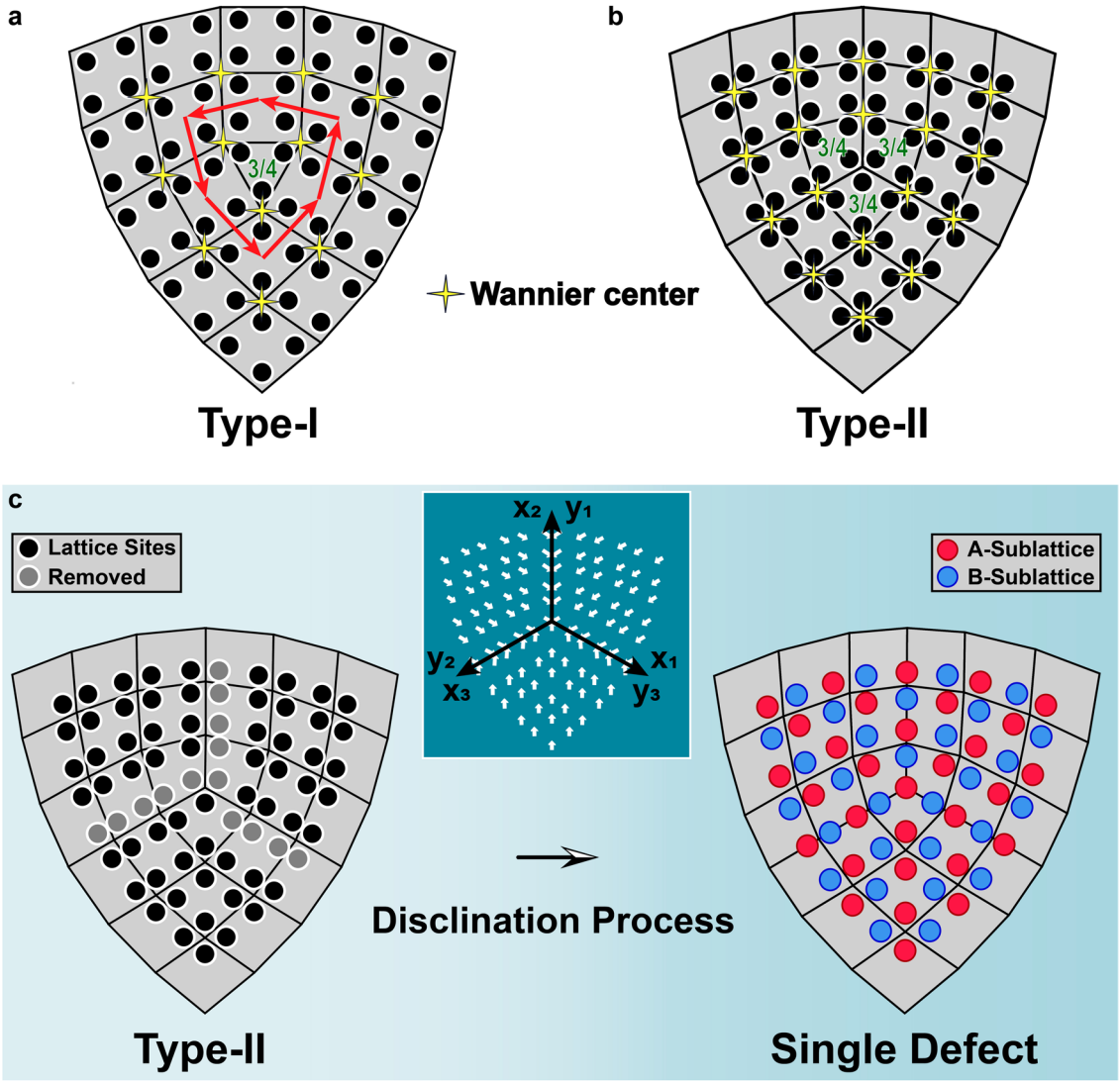

Extended Data Fig. 1 | Realization of C_3-symmetric disclination lattices with a single-site core at the center. a, b Schematics of conventional disclination structures with C_3-symmetry, constructed from a standard 2D SSH model through a 'cutting and gluing' procedure, belonging to type-I (**a**) and type-II (**b**) classifications[23]. Shaded gray quadrilaterals highlight the unit cells, where the yellow stars correspond to the Wannier centers, the black circles are lattice sites, and the red arrows illustrate the calculations of the Frank angle Ω for the type-I lattice[20]. **c** Illustration of the disclination process used to realize a single-site-core C_3-lattice from the associated type-II disclination structure. Gray circles mark the waveguides removed from the original type-II lattice array, red and blue dots are lattice sites for A and B sublattices, respectively, and the white arrows in the upper middle inset indicate the shifting and merging directions. Such a constructed disclination lattice still features chiral symmetry.

https://doi.org/10.1038/s41566-024-01564-2

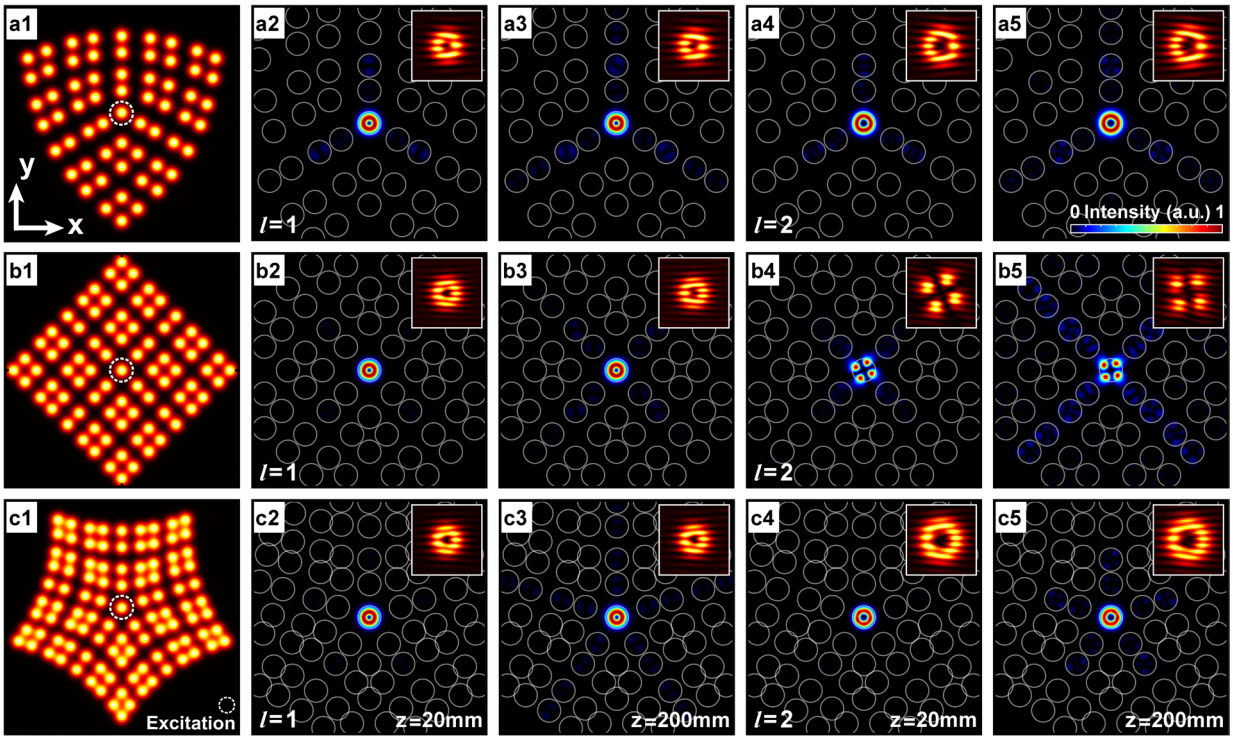

Extended Data Fig. 2 | Numerical simulations of the topological vortex guide by chiral-symmetric disclinations. Propagation of the probe vortex is simulated under single-site excitation at the core (circled in **a1-c1**) of C_3, C_4 and C_5-symmetric disclination lattices. **a1** C_3 disclination lattice. **a2-a5** Output intensity distributions of an $l = 1$ (**a2, a3**) and $l = 2$ (**a4, a5**) vortex beam from the lattice at selected distances $z = 20$ mm (**a2, a4**) and 200 mm(**a3, a5**), highlighting the protected topological vortex transport. Insets are the corresponding numerical interferograms, showing the phase singularity from fringe bifurcations. **b1-b5** Same layout as in **a1-a5** but for the C_4-symmetric lattice. In this case, the $l = 1$ vortex is 'doubly' protected by topology, while the $l = 2$ vortex is not protected due to the lack of real-space topological protection depicted in Fig. 4 of the main text, breaking into a quadruple-like structure at the core with 'tails' populating both sublattices. **c1-c5** Same layout as in **a1-a5** but for the C_5-symmetric lattice, which shows again robust transport for both $l = 1$ and $l = 2$ vortices because they satisfy the requirement of vorticity-coordinated rotational symmetry.

https://doi.org/10.1038/s41566-024-01564-2

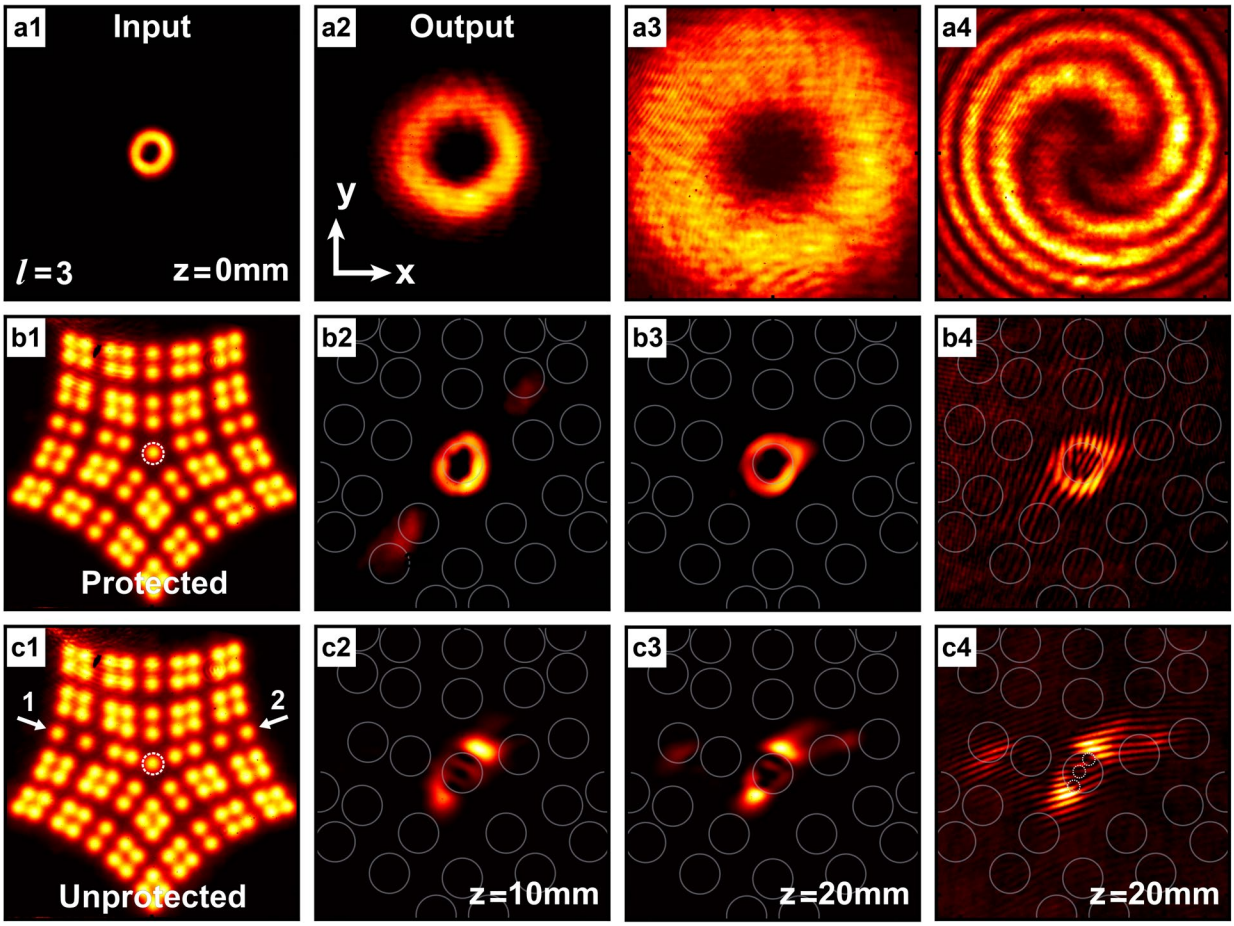

Extended Data Fig. 3 | Experimental results showing the comparison between topologically protected and unprotected transport of a high-order ($l = 3$) vortex. a1 Input intensity pattern of the $l = 3$ vortex beam. **a2-a3** Output intensity patterns after free propagation (in the crystal without lattice structure) taken at (**a2**) 10-mm and (**a3**) 20-mm propagation distances, exhibiting diffraction. **a4** Interferogram of the pattern in (**a3**) with a spherical wave, displaying the high-order vorticity. **b1** A laser-written nontrivial C_5 disclination structure featuring twofold topological protection. **b2-b4** Topologically protected output results obtained from the nontrivial disclination, presenting guided output with preserved vorticity. **c1-c4** Corresponding results from a deformed C_5 disclination structure (**c1**), where the lattice parameters (for the dimer chains along two marked directions) are tuned intentionally so as the two-fold topological protection is disrupted. The lattice parameter tuning leads to the VRS breaking since the rotational symmetry is no longer satisfied. As the propagation distance increases, the vortex beam breaks up and disintegrates into multiple low-order vortices (marked by small dashed circles in **c4**).

https://doi.org/10.1038/s41566-024-01564-2

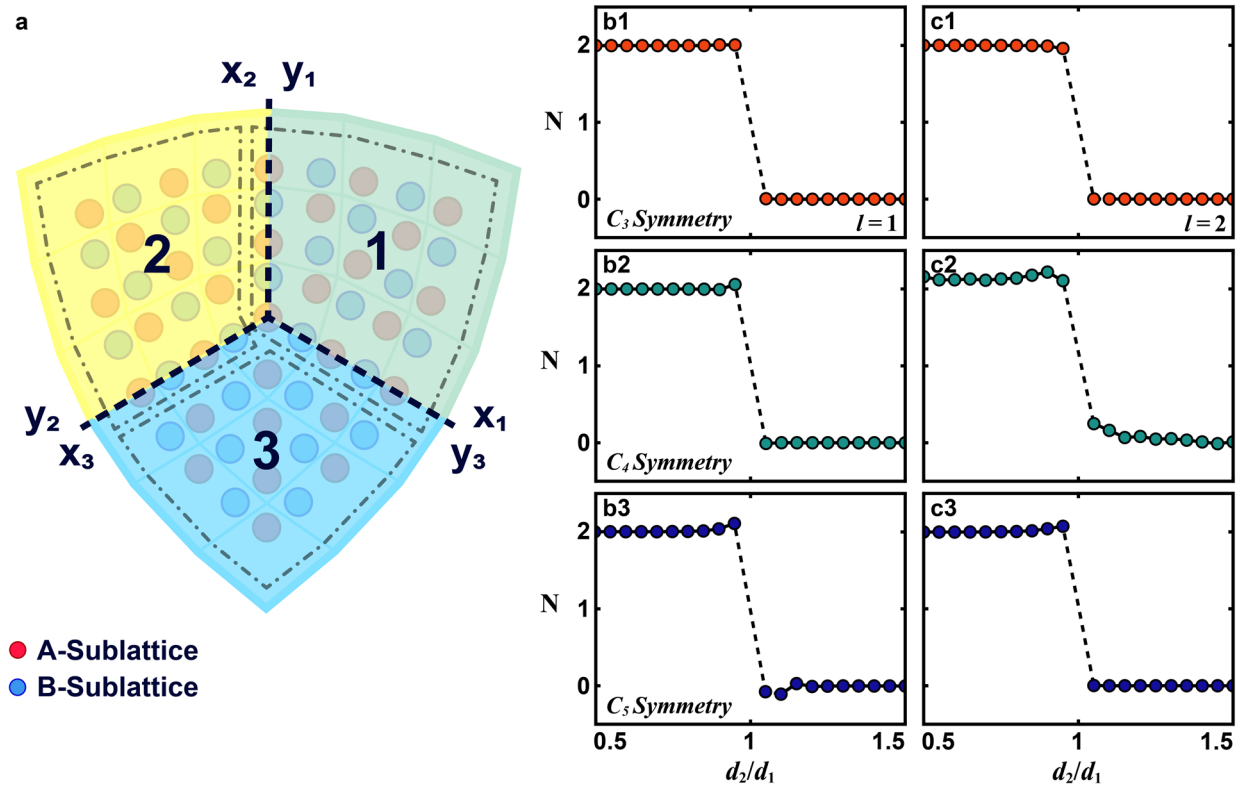

Extended Data Fig. 4 | Generalized multipole chiral numbers used for describing the topological phase of C_n-symmetric disclination lattices. a Schematic illustration showing the definition of coordinate axes in the three groups of a nontrivial C_3-symmetric disclination lattice marked by dash-dotted lines. **b1, c1** Topological invariant of the multipole chiral number N, calculated for a C_3-symmetric disclination lattice and for the $l = 1$ (**b1**) and $l = 2$ (**c1**) vortex modes. **b2, c2** Corresponding calculations for a C_4-symmetric lattice, and **b3, c3** for a C_5-symmetric lattice.

https://doi.org/10.1038/s41566-024-01564-2

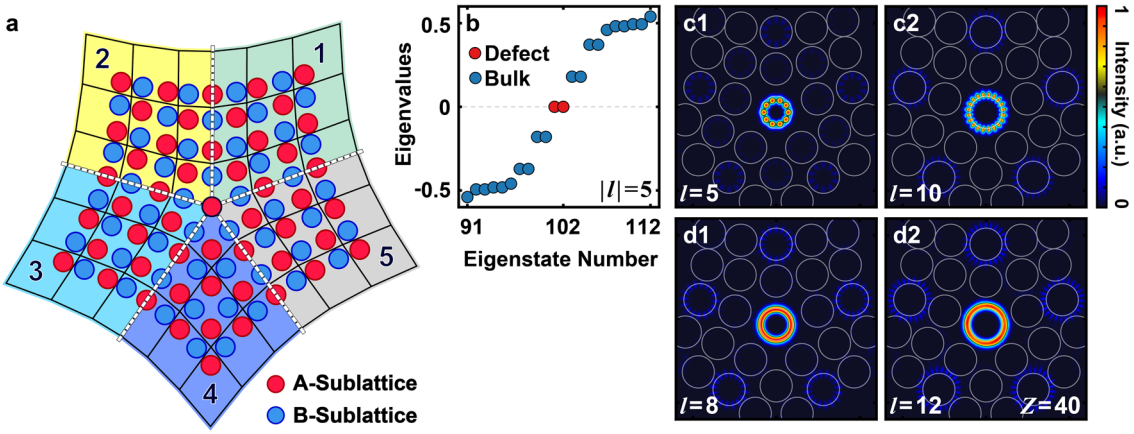

Extended Data Fig. 5 | Protected and unprotected high-order vortex modes in a C_5-symmetric disclination lattice. a Schematic illustration of the chiral-symmetric C_5-disclination lattice. **b** Calculated eigenvalues for the $|l| = 5$ vortex modes of the lattice, where two degenerate defect modes appear right at zero energy but with opposite phase vorticity. **c1, c2** Two examples showing *unprotected* high-order vortex modes with topological charge $l = 5$ (**c1**) and $l = 10$ (**c2**) after a propagation distance $Z = 40$ (simulation from the tight-binding model). In these cases, the vorticity-coordinated rotational symmetry (VRS) is not satisfied because $2l/n$ is an integer. **d1, d2** Two examples showing *protected* high-order vortex modes with topological charge $l = 8$ (**d1**) and $l = 12$ (**d2**). Here, the VRS is satisfied because $2l/n$ is not an integer. These results for different high-order vortices in the same disclination structure further validate the real-space topological protection pictured in Fig. 4 of the main text.

https://doi.org/10.1038/s41566-024-01564-2

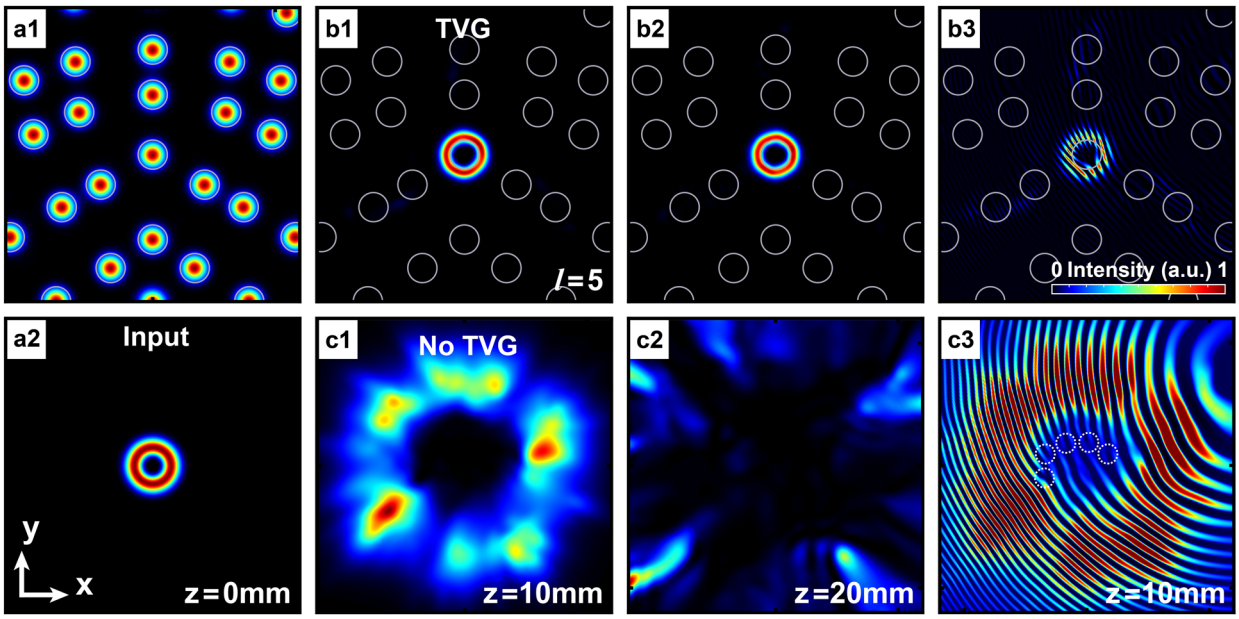

Extended Data Fig. 6 | Comparison of a guided high-order vortex in TVG (top) vs. unguided propagation with vortex splitting in free space (bottom) under perturbation. a1 Intensity distribution of C_3-disclination lattice. **a2** Intensity pattern of a high-order vortex beam with topological charge $l = 5$ at the onset distance. **b1-b2** Output intensity after propagation in the C_3-disclination lattice under background perturbation, selected at (**b1**) 10 mm and (**b2**) 20 mm, highlighting that the $l = 5$ vortex is well-guided without breakup through the TVG. **b3** Interferogram from the guided vortex corresponding to (**b1**), indicating that the high-order phase vorticity remains intact. **c1-c3** Same layout as b1-b3 when the $l = 5$ vortex propagates in free space (without the disclination structure) under the same background noise. The vortex beam experiences significant expansion and distortion, in both intensity and phase profiles: in particular, the interferogram of (c3) exhibits clearly vortex splitting into multiple $l = 1$ phase singularities, marked by 5 dashed circles.